Monthly Notices
of the
ROYAL ASTRONOMICAL SOCIETY

MNRAS **500,** 2461–2474 (2021)
Advance Access publication 2020 October 27

doi:10.1093/mnras/staa3332

EPIC 216747137: a new HW Vir eclipsing binary with a massive sdOB primary and a low-mass M-dwarf companion

R. Silvotti [1]★ V. Schaffenroth,[2] U. Heber,[3] R. H. Østensen,[4] J. H. Telting,[5] J. Vos,[2] D. Kilkenny,[6] L. Mancini [1,7,8] S. Ciceri,[9] A. Irrgang[3] and H. Drechsel[3]

[1]*INAF – Osservatorio Astrofisico di Torino, Strada dell'Osservatorio 20, I-10025 Pino Torinese, Italy*
[2]*Institute of Physics and Astronomy, University of Potsdam, Karl-Liebknecht-Str. 24-25, D-14476 Potsdam, Germany*
[3]*Dr. Remeis-Sternwarte and ECAP, Astronomical Institute, University of Erlangen-Nürnberg, Sternwartstr. 7, D-96049 Bamberg, Germany*
[4]*Department of Physics, Astronomy and Materials Science, Missouri State University, 901 S. National, Springfield, MO 65897, USA*
[5]*Nordic Optical Telescope, Rambla José Ana Fernández Pérez 7, E-38711 Breña Baja, Spain*
[6]*Department of Physics and Astronomy, University of the Western Cape, Private Bag X17, Bellville 7535, South Africa*
[7]*Department of Physics, University of Rome 'Tor Vergata', Via della Ricerca Scientifica 1, I-00133 Roma, Italy*
[8]*Max Planck Institute for Astronomy, Königstuhl 17, D-69117 Heidelberg, Germany*
[9]*Department of Astronomy, Stockholm University, SE-106 91 Stockholm, Sweden*

Accepted 2020 October 18. Received 2020 October 16; in original form 2020 October 1

ABSTRACT

EPIC 216747137 is a new HW Virginis system discovered by the *Kepler* spacecraft during its *K*2 'second life'. Like the other HW Vir systems, EPIC 216747137 is a post-common-envelope eclipsing binary consisting of a hot subluminous star and a cool low-mass companion. The short orbital period of 3.87 h produces a strong reflection effect from the secondary (∼9 per cent in the *R* band). Together with AA Dor and V1828 Aql, EPIC 216747137 belongs to a small subgroup of HW Vir systems with a hot evolved sdOB primary. We find the following atmospheric parameters for the hot component: $T_{\rm eff} = 40400 \pm 1000$ K, $\log g = 5.56 \pm 0.06$, and $\log(N({\rm He})/N({\rm H})) = -2.59 \pm 0.05$. The sdOB rotational velocity $v \sin i = 51 \pm 10$ km s^{-1} implies that the stellar rotation is slower than the orbital revolution and the system is not synchronized. When we combine photometric and spectroscopic results with the *Gaia* parallax, the best solution for the system corresponds to a primary with a mass of about 0.62 $M_\odot$ close to, and likely beyond, the central helium exhaustion, while the cool M-dwarf companion has a mass of about 0.11 $M_\odot$.

Key words: binaries: eclipsing – stars: horizontal branch – stars: individual: EPIC 216747137.

1 INTRODUCTION

Post-common-envelope binaries (PCEBs) are crucial to study the poorly understood and short-lived common-envelope (CE) phase of stellar evolution.

Among PCEBs, HW Virginis stars are a specific class of eclipsing binaries consisting of a hot subdwarf primary with an M-dwarf companion (see Heber 2016 for a recent review on hot subdwarf stars). There are two subgroups of HW Vir stars: those similar to the prototype, with a core-helium-burning sdB (subdwarf B) primary, located in the extreme horizontal branch (EHB) part of the H-R diagram. And those like AA Dor, with a hotter and more evolved primary of sdOB spectral class, beyond the central helium exhaustion.

The possibility of measuring accurate dynamical masses in HW Virginis systems is important to shed light on the formation mechanism of hot subdwarfs. These stars are characterized by very thin hydrogen envelopes and masses close to the canonical mass of 0.47 $M_\odot$.

To form such an object, the hydrogen envelope of the red giant progenitor must be removed almost completely. Han et al. (2002, 2003, see also Clausen et al. 2012) describe three main binary evolution scenarios to form an sdB star: (i) CE ejection, (ii) stable Roche lobe overflow (RLOF), and (iii) the merger of two He white dwarfs (WD). The latter scenario may contribute only for a very small fraction of sdBs given that the high masses and high rotation rates foreseen are not supported by the observations (Fontaine et al. 2012; Charpinet et al. 2018; Reed et al. 2018). Since ∼50 per cent of the non-composite-spectrum hot subdwarfs are members of short-period binaries with orbital periods between 0.027 and ∼30 d (Maxted et al. 2001; Napiwotzki et al. 2004; Kupfer et al. 2015, 2020), mostly with a WD or an M-type main-sequence (MS) companion, CE ejection triggered by a close companion is generally regarded as the main formation channel. As far as the RLOF scenario is concerned, an important recent work by Pelisoli et al. (2020) shows that almost all the wide binaries with K- to F-type MS companions that they analysed show evidence of previous interaction, confirming that the RLOF is another efficient way to form ∼30–40 per cent of hot subdwarfs, and suggesting that binary interaction may *always* be required to form a hot subdwarf star. Indeed, Stark & Wade (2003) found that ∼40 per cent of hot subdwarfs have colours consistent with

★ E-mail: roberto.silvotti@inaf.it

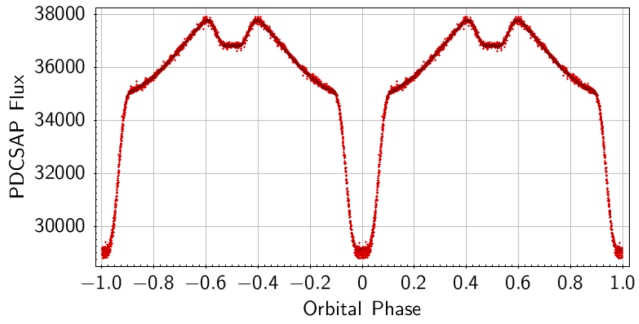

Figure 1. K2 light curve.

the presence of an unresolved late-type companion in a magnitude-limited sample (or ∼30 per cent in a volume-limited sample). Putting these numbers together, we can estimate that ∼35 per cent of hot subdwarfs are in close binaries with M-dwarf or WD companions, while ∼30 per cent are in wide binaries with F/G/K companions.

However, the remaining fraction of ∼35 per cent consists of apparently single hot subdwarfs. For them, different formation mechanisms have been invoked, including the merger of a He WD with a low-mass hydrogen-burning star (Clausen & Wade 2011). The presence of a substellar companion, difficult to detect, orbiting the sdB progenitor is another possibility (Soker 1998; Han et al. 2012), only partially supported by the observations.

On the one hand, no planets transiting hot subdwarfs were found in a large survey with the Evryscope, capable of detecting planets with radii slightly smaller than Jupiter (Ratzloff et al. 2020). Neither were planetary transits of hot subdwarfs found up to now by the *Kepler*/*K*2 or the *TESS* space missions. Moreover, no significant radial velocity (RV) variations were found from high-accuracy Harps-N measurements of a small sample of eight bright apparently single sdB stars (Silvotti, Østensen & Telting 2020), excluding the presence of close substellar companions down to a few Jupiter masses and, for half of these stars, excluding also the presence of higher mass companions in wide orbits. These null results do not exclude that the planets were completely destroyed during the CE phase or that their envelope was removed leaving a very small and dense planetary core, difficult to detect (see e.g. the controversial cases of KIC 5807616 and KIC 10001893, Charpinet et al. 2011; Silvotti et al. 2014).

On the other hand, there are at least three known HW-Vir systems with brown dwarf (BD) companions having masses between 0.04 and 0.07 $M_{\odot}$ (Geier et al. 2011; Schaffenroth et al. 2014, 2015), plus two more with masses close to the hydrogen-burning limit (Schaffenroth et al. 2019, figs 14 and 15). And there are a few controversial cases of planet detections through the eclipse or pulsation timing method (see e.g. Baran, Bachulski & Curyło 2016, and references therein).

Thanks to the high number of new HW-Vir systems discovered recently from the light curves of the OGLE and ATLAS projects (Schaffenroth et al. 2019), and the new ones that are being discovered by the *TESS* mission, the number of HW-Vir systems with substellar companions is likely to grow significantly in the short term. With enough statistics, it should be possible to determine the minimum mass for a substellar companion to eject the red giant envelope and survive engulfment. According to theory, it was thought that this limit could be near 10 M_{Jup} (Soker 1998; Han et al. 2012), but a recent article suggests that this mass limit could be higher, around 30–50 M_{Jup} (Kramer et al. 2020).

The system described in this paper, EPIC 216747137 (alias UCAC2 23234937), is a new HW-Vir binary relatively bright (*Gaia* DR2 magnitude $G = 13.767 \pm 0.004$), located about 880 pc from us (*Gaia* DR2 parallax of 1.14 ± 0.06 mas). The eclipsing system was independently discovered by Mariusz Bajer on 2019 February 8 and the discovery was published in the Variable Star Index data base under the name BMAM-V272. In the next sections, we present the results of an analysis of both photometric and spectroscopic data of EPIC 216747137, that allow us to infer the orbital parameters of the system and the main characteristics of the primary and secondary components. The eclipsing system was independently discovered by Mariusz Bajer on February 8, 2019 and the discovery was published in the Variable Star Index database under the name BMAM-V272.[1]

2 TIME-SERIES PHOTOMETRY

2.1 *K2* discovery

EPIC 216747137 was observed by the *Kepler* space telescope during cycle 7 of its *K*2 secondary mission in long-cadence mode, with a sampling time of 29.42 min. We downloaded the data from the 'Barbara A. Mikulski Archive for Space Telescopes' (MAST)[2] and we used the PDCSAP fluxes (PDC=Presearch Data Conditioning, SAP=Simple Aperture Photometry, see *K*2 documentation for more details). After having removed some bad data point (those with SAP_QUALITY flag different from zero or 2048 plus two outliers), the data set we used, as shown in Fig. 1, consists of 81.3 d from BJD_{TBD} 2457301.48620 to 2457382.80453 (corresponding to 2015 October 05–December 26).

2.2 SAAO BVR data

EPIC 216747137 was re-observed at the Sutherland site of the South African Astronomical Observatory (SAAO) using the 1-m Elizabeth telescope with the STE3 CCD photometer which has a readout time of about 6 s (pre-binned 2 × 2), small compared to the exposure times for filters *B* (60 s), *V* (30 s), and *R* (30 s). Observations were made using each filter on a separate night (2017 May 18, 17, and 19, respectively) to maximize the resolution of the light curve. Reduction of the CCD frames, magnitude extraction by profile-fitting, and differential correction using several field stars were performed using software written by Darragh O'Donoghue and partly based on the DoPHOT program described by Schechter, Mateo & Saha (1993).

The *BVR* light curves are shown in Fig. 2. Comparing Fig. 1 with Fig. 2, we immediately note the different shape and depth of the primary and secondary eclipses, due to the smearing caused by the poor sampling rate of the *K*2 long-cadence data. In Fig. 1, the primary and secondary eclipses have a depth of ∼17 per cent and less than 3 per cent respectively, while they are much deeper in the SAAO data (∼39 per cent and ∼8 per cent in the *R* band). For this reason, the *K*2 data were used only to improve the ephemeris, while the analysis of the light curve was performed using the ground-based photometry.

3 RADIAL VELOCITIES

EPIC 216747137 was observed spectroscopically with various instruments. As a first step, in order to measure the RVs of the primary, nine high-resolution spectra were obtained at different orbital phases in 2016 July and September using FEROS with the 2.2-m MPG/ESO telescope at La Silla Observatory in Chile,

[1] http://www.aavso.org/vsx/index.php?view=detail.top&oid=684233
[2] archive.stsci.edu

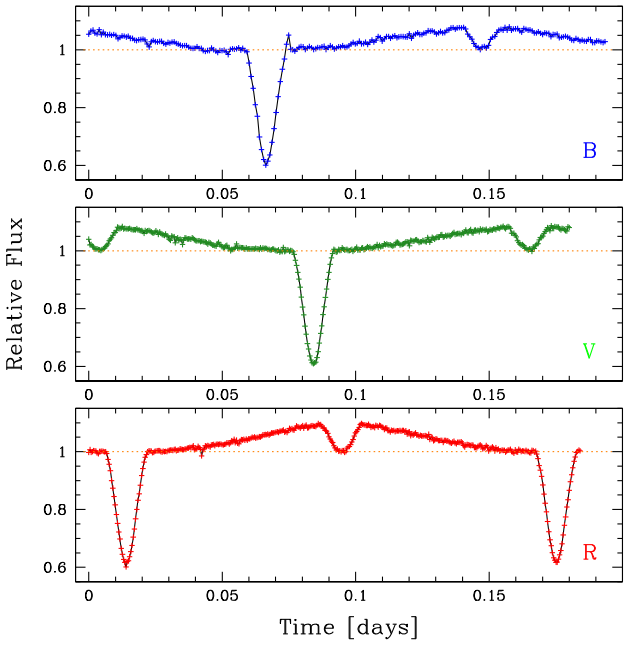

Figure 2. SAAO BVR light curves. The flux is normalized to the level just before and just after the primary eclipse.

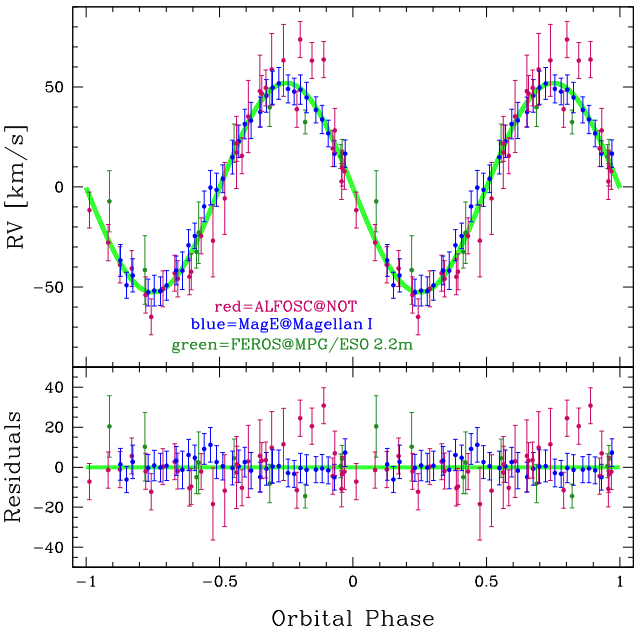

Figure 3. Radial velocities.

with exposure times of 1800 s.[3] The FEROS spectra were reduced using CERES, a pipeline written for échelle spectrographs described in Brahm, Jordán & Espinoza (2017). The raw spectra were first corrected with calibration frames obtained in the afternoon or during twilight, and then calibrated in wavelength using a Th–Ar spectrum. The RVs of the sdOB star were measured from the He II line at 4686 Å, while the Balmer lines were not used because they give more noisy results. However, the results were quite poor due to the low signal-to-noise ratio of the FEROS spectra.

For this reason, new observations were carried out as part of our *K*2 sdBV follow-up spectroscopic survey (Telting et al. 2014). We obtained 32 low-resolution spectra ($R \sim 2000$, or 2.2 Å) in two runs (22 spectra in 2017 July, 10 spectra 2018 between March and August) at the 2.56-m Nordic Optical Telescope (NOT, La Palma) using ALFOSC, 600 s exposure times, grism no. 18, 0.5 arcsec slit, and CCD no. 14, giving an approximate wavelength range 345–535 nm. The spectra were homogeneously reduced and analysed. Standard reduction steps within IRAF include bias subtraction, removal of pixel-to-pixel sensitivity variations, optimal spectral extraction, and wavelength calibration based on helium arc-lamp spectra. The peak signal-to-noise ratio of the individual spectra ranges from 50 to 125. The RVs were measured using the lines Hβ, Hγ, Hδ, H8, and H9 through a cross-correlation analysis in which we used as a template a synthetic fit to an orbit-corrected average (all spectra shifted to zero velocity before averaging).

Finally, 32 medium-resolution spectra were obtained with MagE@Magellan I at Las Campanas Observatory in Chile in 3.5 h on 2017 September 17, with 300 s exposure times, 1 arcsec slit, $R \sim 4100$ and a useful wavelength range of 3500–8100 Å. The typical signal-to-noise ratios were between 80 and 110. The spectra were reduced using the MagE pipeline (Kelson et al. 2000; Kelson 2003). The RVs were measured using Balmer lines and two He I lines at 4471 and 5875 Å.

[3]For the first two spectra we used 1000 and 1500 s.

The RV measurements obtained from the MagE spectra are the most accurate due to the best compromise between high SN ratio, relatively high resolution and short exposure times, which means lower smearing. However, the ALFOSC and FEROS RVs were also used using appropriate weights (Fig. 3). From the best RV fit, we obtain a circular orbit with an RV amplitude $K = 52.3 \pm 1.3$ km s^{-1}, and a system velocity $v_0 = -6.4 \pm 1.2$ km s^{-1}. Smearing is not considered as it is negligible for MagE and ALFOSC spectra (0.08 per cent and 0.3 per cent, respectively) and has little importance only for FEROS spectra (3 per cent). By fitting all the 73 RVs listed in Table 1 with an eccentric solution, we can constrain the eccentricity to a value smaller than 0.091.[4]

Both the ALFOSC and MagE spectra were used not only to measure the RVs, but also to derive accurate atmospheric parameters and the rotational velocity of the sdOB star and to measure their variations as a function of the orbital phase, as described in the next section.

4 ATMOSPHERIC PARAMETERS AND ROTATIONAL VELOCITY OF THE PRIMARY

The reflection effect adds additional light to the sdOB spectrum, which varies with phase. Because we cannot model this contribution, each individual spectrum is matched separately to a grid of synthetic models to derive the effective temperature, gravity, and helium abundance. If the contribution to the spectrum of the primary is significant, the resulting atmospheric parameters should show trends with orbital phase as a consequence of the varying light pollution. Indeed, such apparent variations of atmospheric parameters have been found in other reflection binaries such as HW Vir (Wood & Saffer 1999), HS 0705+6700 (Drechsel et al. 2001), and most distinctively in HS 2333+3937 (Heber et al. 2004). The best estimate of the atmospheric parameters comes from data taken during secondary

[4]We obtain an eccentricity of 0.019 ± 0.024, which translates into a 3σ upper limit of 0.091.

Table 1. RV measurements.

BJD_{TDB} –2450000.	RV (km s^{-1})	Error (km s^{-1})	Instr.	UT date
7590.682242	11.14	6.64	FEROS	2016-07-21
7590.755434	–38.47	8.18	FEROS	2016-07-21
7645.521343	–28.90	15.42	FEROS	2016-09-14
7645.542780	15.74	9.59	FEROS	2016-09-14
7645.564206	33.73	9.60	FEROS	2016-09-14
7645.585628	26.38	6.00	FEROS	2016-09-14
7645.607066	9.17	6.00	FEROS	2016-09-14
7645.628503	–13.21	15.33	FEROS	2016-09-14
7645.649944	–47.56	17.09	FEROS	2016-09-14
7958.472032	–51.96	9.00	ALFOSC	2017-07-23
7958.479132	–50.91	9.00	ALFOSC	2017-07-23
7958.486222	–30.49	9.00	ALFOSC	2017-07-23
7958.493322	–32.92	18.00	ALFOSC	2017-07-23
7958.500422	–11.79	18.00	ALFOSC	2017-07-24
7958.507522	11.19	18.00	ALFOSC	2017-07-24
7958.514612	29.18	18.00	ALFOSC	2017-07-24
7958.521712	41.84	18.00	ALFOSC	2017-07-24
7958.528812	52.66	18.00	ALFOSC	2017-07-24
7958.535902	57.18	18.00	ALFOSC	2017-07-24
7958.565612	13.15	9.00	ALFOSC	2017-07-24
7958.572712	1.74	9.00	ALFOSC	2017-07-24
7958.579812	–17.64	9.00	ALFOSC	2017-07-24
7958.591172	–33.85	9.00	ALFOSC	2017-07-24
7958.598262	–44.95	9.00	ALFOSC	2017-07-24
7958.605362	–46.79	9.00	ALFOSC	2017-07-24
7960.478821	67.59	9.00	ALFOSC	2017-07-25
7960.485921	57.11	9.00	ALFOSC	2017-07-25
7960.493021	57.61	9.00	ALFOSC	2017-07-25
7960.549991	–70.95	9.00	ALFOSC	2017-07-26
7960.557091	–56.91	9.00	ALFOSC	2017-07-26
7960.564181	–49.15	9.00	ALFOSC	2017-07-26
8014.490569	–42.73	7.92	MagE	2017-09-17
8014.494309	–55.17	6.49	MagE	2017-09-17
8014.498039	–50.28	8.30	MagE	2017-09-17
8014.507289	–58.76	6.72	MagE	2017-09-18
8014.511029	–57.84	7.66	MagE	2017-09-18
8014.514759	–58.11	7.13	MagE	2017-09-18
8014.518489	–55.26	7.36	MagE	2017-09-18
8014.524279	–47.81	7.19	MagE	2017-09-18
8014.528019	–47.87	9.37	MagE	2017-09-18
8014.531749	–35.15	7.80	MagE	2017-09-18
8014.535489	–30.53	6.37	MagE	2017-09-18
8014.541189	–15.77	7.71	MagE	2017-09-18
8014.544929	–6.39	8.64	MagE	2017-09-18
8014.548659	–7.49	8.26	MagE	2017-09-18
8014.552399	–1.96	6.91	MagE	2017-09-18
8014.558219	8.82	8.43	MagE	2017-09-18
8014.561949	16.75	8.10	MagE	2017-09-18
8014.565679	25.39	7.44	MagE	2017-09-18
8014.569419	27.14	9.01	MagE	2017-09-18
8014.574989	31.38	7.49	MagE	2017-09-18
8014.578729	39.47	8.14	MagE	2017-09-18
8014.582469	43.56	8.29	MagE	2017-09-18
8014.586199	45.64	7.96	MagE	2017-09-18
8014.591779	42.95	6.97	MagE	2017-09-18
8014.595519	41.63	6.68	MagE	2017-09-18
8014.599249	42.56	7.36	MagE	2017-09-18
8014.602999	38.63	7.62	MagE	2017-09-18
8014.608619	32.41	6.52	MagE	2017-09-18
8014.612359	27.67	7.08	MagE	2017-09-18
8014.616089	20.70	6.67	MagE	2017-09-18
8014.619829	10.60	6.42	MagE	2017-09-18
8014.626199	10.55	6.89	MagE	2017-09-18
8201.763003	32.78	9.00	ALFOSC	2018-03-24
8211.685742	–48.44	9.00	ALFOSC	2018-04-03
8268.635281	3.39	9.00	ALFOSC	2018-05-30
8269.702361	9.53	9.00	ALFOSC	2018-05-31
8304.505900	40.62	9.00	ALFOSC	2018-07-05
8304.596910	–60.01	9.00	ALFOSC	2018-07-05
8307.568760	43.45	9.00	ALFOSC	2018-07-08
8312.607699	–3.29	9.00	ALFOSC	2018-07-13
8338.477179	15.78	9.00	ALFOSC	2018-08-07
8338.536299	22.17	11.10	ALFOSC	2018-08-08

eclipse and just before and after primary eclipse, when the light pollution should be lowest.

We closely follow the analysis strategy outlined by Heber et al. (2004). The Balmer and helium lines in the ALFOSC and MagE spectra are used to determine effective temperature, gravity and helium abundance, and the projected rotation velocity $v \sin i$. Because the spectral resolution of the ALFOSC spectra is insufficient for $v \sin i$ to be determined, the latter is derived from the MagE spectra. The ALFOSC spectra show the entire Balmer series with a well defined continuum and can, therefore, be used to determine $T_{\rm eff}$, log g, and log $y = \log(N({\rm He})/N({\rm H}))$. For the MagE spectra, their wavy run of the continuum prohibits the Balmer lines to be used. However, they are very useful to derive the projected rotation velocity and allow us to investigate the helium ionization equilibrium including lines not covered by the ALFOSC spectral range, from which an independent estimate of the effective temperature can be obtained. Since the helium lines are quite insensitive to gravity, the gravity had to be fixed in the analysis of the MagE spectra to log $g = 5.56$ derived from the ALFOSC spectra. We match the Balmer (Hβ to H 11) and He I (4471 and 4026 Å), as well as He II 4686 and 4542 Å line profiles in the ALFOSC spectra, and He I (4471 and 5875 Å) and He II (4686 and 5411 Å) lines in the MagE spectra with a grid of synthetic spectra.

The models are computed using three codes. First, the ATLAS12 code (Kurucz 1996) is used to compute the atmospheric structure (temperature/density stratification) in LTE (local thermodynamic equilibrium). Non-LTE population numbers are then calculated with the DETAIL code (Giddings 1981) and the coupled equations of radiative transfer and statistical equilibrium are solved numerically. In the final step, the SURFACE code (Giddings 1981) computes the emergent spectrum based on the non-LTE occupation numbers provided by DETAIL. In this step detailed line-broadening tables are incorporated. All three codes have been updated recently (see Irrgang et al. 2018). The impact of departures from LTE for hydrogen and helium on the atmospheric structure is modelled by feeding back population numbers calculated by DETAIL to ATLAS12 and iterate. In addition, the occupation probability formalism (Hubeny, Hummer & Lanz 1994) for hydrogen has been implemented and line broadening tables have been updated. Stark broadening tables for hydrogen and neutral helium are taken from Tremblay & Bergeron (2009) and Beauchamp, Wesemael & Bergeron (1997), respectively. The broadening of the lines of ionized helium was treated as described by Auer & Mihalas (1972).

The observed spectra are matched to the model grid by χ^2 minimization as described by Saffer et al. (1994) using implementations

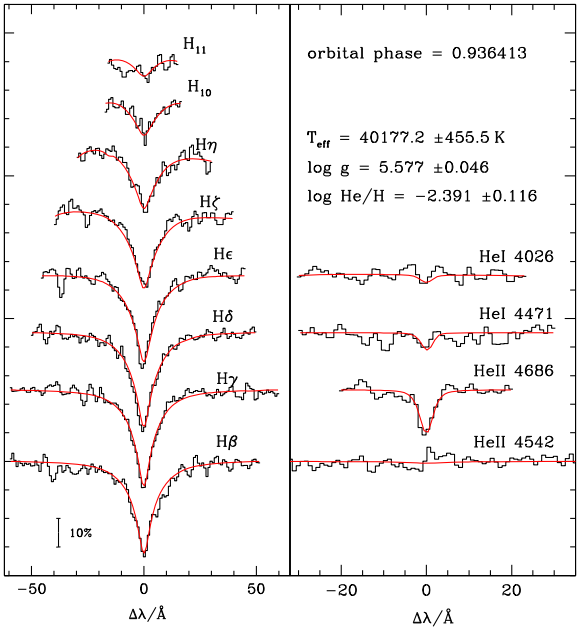

Figure 4. Fit of one of the ALFOSC spectra corresponding to orbital phase 0.9364, close to the primary eclipse, for which the contribution of the secondary is minimum.

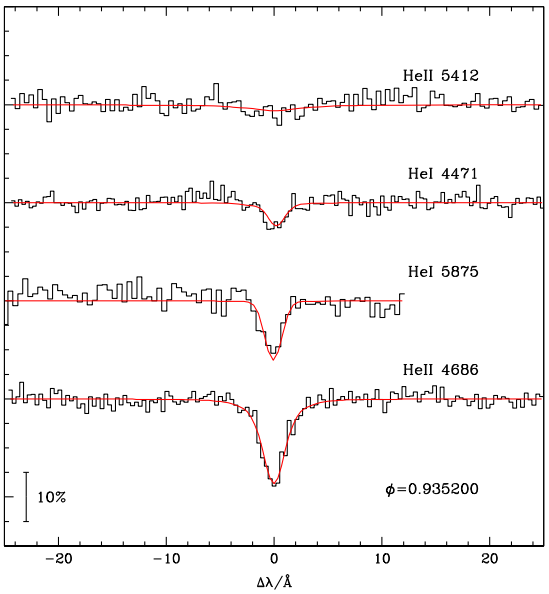

Figure 5. Same as Fig. 4, but for one of the MagE spectra corresponding to orbital phase 0.9352.

by Napiwotzki, Green & Saffer (1999) and Hirsch (2009). Exemplary fits to an ALFOSC and a MagE spectrum are shown in Figs 4 and 5.

The results of the quantitative spectral analysis of all ALFOSC and MagE spectra are summarized in Fig. 6. In the left-hand panels (ALFOSC), the apparent variations of the effective temperature with phase and an amplitude of ∼2500 K are obvious. The lowest temperatures (∼40 kK) occur near primary eclipse and in the secondary eclipse, where the contribution by extra light should be minimal. Hence, the increase during other orbital phases is caused by reflected light and, therefore, not real. Similarly, variations of the helium abundance are observed. The apparent variations of the surface gravity, however, are small. The mean values adopted for $T_{\rm eff}$, $\log g$, and $\log y$, summarized in Table 2, are obtained by selecting six spectra close to the primary eclipse with phase between −0.1 and +0.1 and adding one spectrum at phase 0.52. The analysis of the MagE spectra also results in effective temperatures and helium abundances that seem to vary with orbital phase (cf. Fig. 6, right-hand panels), but with amplitudes less pronounced than those from the ALFOSC spectra. For this reason, we use all the MagE spectra to compute mean values and standard deviations of $T_{\rm eff}$ and $\log y$ (cf. Table 2).

The effective temperature and surface gravity of EPIC 216747137 ($T_{\rm eff}$ = 40400 K and $\log g$ = 5.56) are very similar to the hot HW Vir systems AA Dor (Klepp & Rauch 2011) and V1828 Aql (= NSVS 14256825, Almeida et al. 2012). EPIC 216747137 also shares an underabundance of helium ($\log y = -2.59$) with the two others.

The projected rotational velocity, as derived from the individual MagE spectra (central right panel of Fig. 6), results in a mean $v \sin i = 51 \pm 10\,{\rm km\,s^{-1}}$, significantly less than $\sim$70 km s^{-1} expected for tidally locked rotation. Mean rotational velocity of 51 km s^{-1} and standard deviation of 10 km s^{-1} are obtained excluding only a single outlier close to phase 0 (see central right panel of Fig. 6).

5 STELLAR PARAMETERS: RADIUS, MASS, AND LUMINOSITY

The second data release of *Gaia* provided a precise (5 per cent) parallax measurement which allows the stellar parameters (radius, mass, and luminosity) to be derived from the atmospheric parameters, if the angular diameter were known. The latter can be derived from the spectral energy distribution (SED).

5.1 Angular diameter and interstellar reddening

The angular diameter Θ is derived from the observed flux $f(\lambda)$ and the synthetic stellar surface flux via the relation $f(\lambda) = \Theta^2 F(\lambda)/4$, which means that Θ is just a scaling factor which shifts fluxes up and down. Strictly speaking, the apparent magnitudes of the sdOB can be measured during secondary eclipses only, when the companion is completely eclipsed by the larger subdwarf, because of the contamination by light from the companion's heated hemisphere. Such data are not available. Nevertheless, many photometric measurements are available in different filter systems, covering the spectral range in the optical and infrared. However, those measurements are mostly averages of observations taken at multiple epochs and, therefore, may be subject to light pollution from the companion.

The low Galactic latitude ($b = -9.9^\circ$) implies that interstellar reddening may be large. Therefore the angular diameter has to be determined along with the interstellar colour excess. The reddening law of Fitzpatrick et al. (2019) and a synthetic flux distribution from the grid of model atmospheres described in Section 4 is matched to the observed magnitudes employing a χ^2-based fitting routine (see Heber, Irrgang & Schaffenroth 2018 for details). The final atmospheric parameters and their respective uncertainties derived from the quantitative spectral analysis (see Section 4) are used. Indeed, interstellar reddening is significant with $E(B-V) = 0.213^{+0.010}_{-0.016}$ mag (see Table 3). The latter is consistent with values from reddening maps of Schlegel, Finkbeiner & Davis (1998) and Schlafly & Finkbeiner (2011): 0.253 mag and 0.217 mag, respectively.

Because of light pollution from the companion's heated hemisphere, the resulting angular diameter will be somewhat overestimated, as that is not accounted for in the synthetic SED. Red and infrared magnitudes are expected to be more affected than the blue

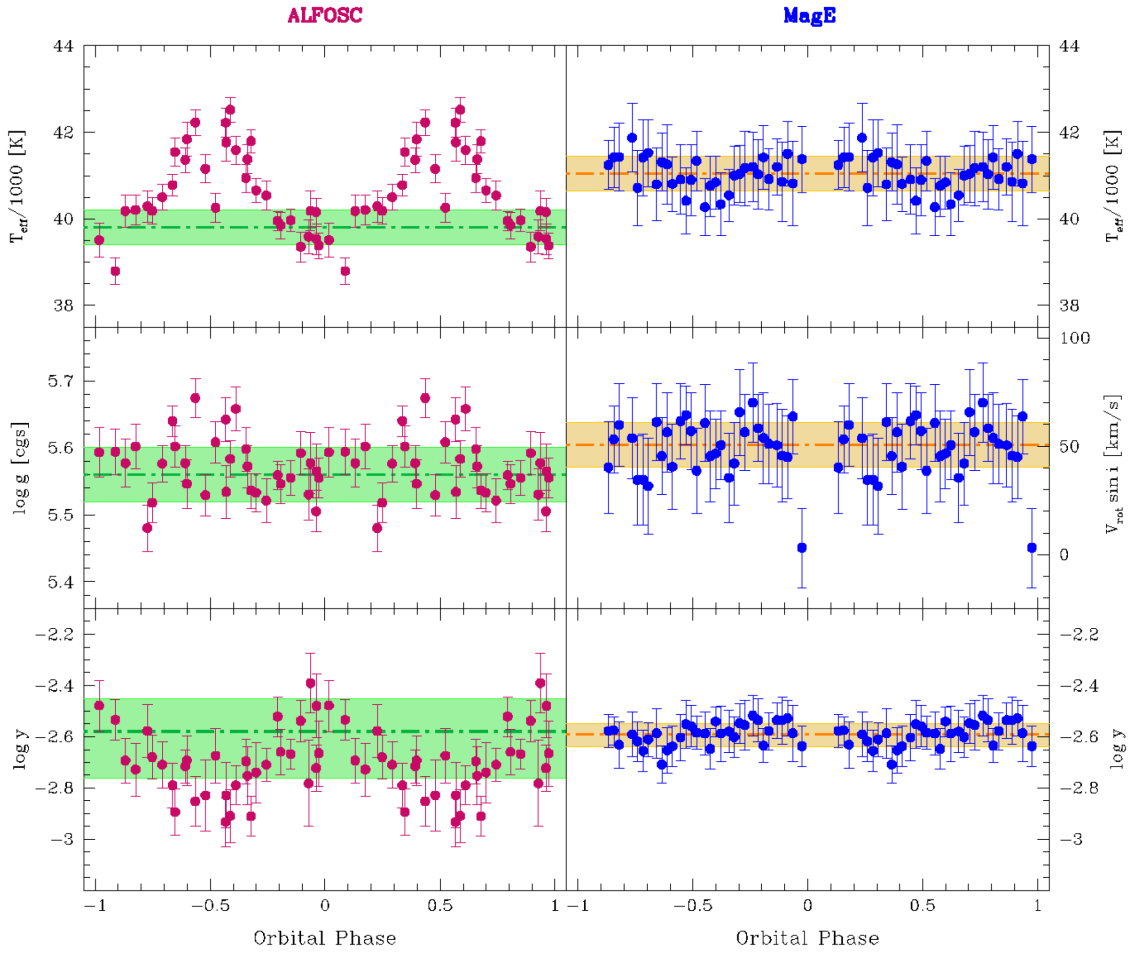

Figure 6. $T_{\rm eff}$, log g, log y, and $v_{\rm rot}$ sin i variations as a function of the orbital phase. Left-hand panels: ALFOSC. The green dotted–dashed horizontal lines mark the adopted $T_{\rm eff}$, log g, and log y and the associated errors (cf. Table 2 and text). Note the two points with low $T_{\rm eff}$ near phase 0.5 (secondary eclipse), when the contribution of the secondary is strongly reduced. Right-hand panels: MagE. The orange dotted–dashed horizontal lines mark the average values and associated errors of $T_{\rm eff}$, $v_{\rm rot}$ sin$i$, and He abundance. In the central panel, note the outlier near phase zero (primary eclipse).

Table 2. SdOB atmospheric parameters and rotational velocity.

	ALFOSC	MagE	Adopted
$T_{\rm eff}$ (K)	39800 ± 400	41000 ± 400	40400 ± 1000
log g (cgs)	5.56 ± 0.04		5.56 ± 0.06
log y	$-2.58^{+0.13}_{-0.18}$	$-2.59^{+0.04}_{-0.05}$	-2.59 ± 0.05
v sin i (km s^{-1})		51 ± 10	51 ± 10

ones. To account for the additional light, we added a blackbody spectrum to the fit, allowing its temperature as well as the relative emission area to vary. The final fit is shown in Fig. 7 and results summarized in Table 3.

5.2 Stellar radius, mass, and luminosity

The *Gaia* DR2 parallax is corrected for a zero-point offset of -0.029 mas as recommended by Lindegren et al. (2018) and applied by Bailer-Jones et al. (2018) to derive distances. By combining it with the atmospheric parameters (log g and $T_{\rm eff}$) and the angular diameter, we can determine the star's radius R, mass M, and luminosity L. The respective uncertainties of the stellar parameters are derived by Monte Carlo error propagation. Results are summarized in Table 3. Once the radius ($R = 0.206 \pm 0.012\,{\rm R}_\odot$)

Table 3. SED + *Gaia* DR2 results.

Atmospheric parameters from spectral analysis	
Effective temperature $T_{\rm eff}$	40400 ± 1000 K
Surface gravity log(g(cm s^{-2}))	5.56 ± 0.06
Helium abundance log y	-2.59 ± 0.05
Parameters from SED fit and *Gaia* DR2 parallax	
Colour excess $E(B-V)$	$0.213^{+0.010}_{-0.016}$ mag
Metallicity z (fixed)	0 dex
Angular diameter log(Θ(rad))	$-10.975^{+0.009}_{-0.015}$
Blackbody temperature $T_{\rm bb}$	2900^{+2600}_{-1300} K
Blackbody surface ratio $A_{\rm eff,\,bb}/A_{\rm eff}$	$2.5^{+4.3}_{-1.4}$
Generic excess noise $\delta_{\rm excess}$ (fixed)	0.033 mag
Parallax ϖ (RUWE=1.04, offset=0.029 mas)*	1.14 ± 0.06 mas
$R = \Theta/(2\varpi)$	$0.206 \pm 0.012\,{\rm R}_\odot$
$M = gR^2/G$	$0.56^{+0.11}_{-0.10}\,{\rm M}_\odot$
$L/L_\odot = (R/R_\odot)^2(T_{\rm eff}/T_{\rm eff,\,\odot})^4$	100^{+16}_{-15}

Notes: * We use the RUWE parameter as a quality indicator, best is 1, <1.4 is acceptable, 1.04 is good.

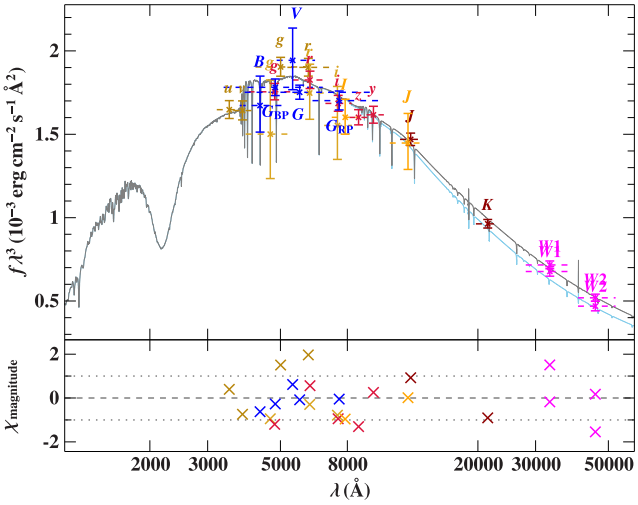

Figure 7. Comparison of synthetic and observed photometry (flux times wavelength to the power of 3): top panel: SED, filter-averaged fluxes converted from observed magnitudes. Dashed horizontal lines depict the approximate width of the respective filters (widths at tenth maximum). The best-fitting model, smoothed to a spectral resolution of 6 Å, is shown in grey. Bottom panel: residual χ, difference between synthetic and observed magnitudes divided by the corresponding uncertainties. The different photometric systems are assigned the following colours: SDSS (APASS, golden; Alam et al. 2015), SkyMapper (golden; Wolf et al. 2018; Onken et al. 2019), PAN-STARRS (red; Chambers & et al. 2017), Johnson (APASS, blue; Henden et al. 2015), *Gaia* (blue; Evans et al. 2018 with corrections and calibrations from Maíz Apellániz & Weiler 2018), DENIS (yellow; Fouqué et al. 2000), VHS-DR6 (brown; Lawrence et al. 2007), and *WISE* (magenta; Wright et al. 2010; Schlafly, Meisner & Green 2019).

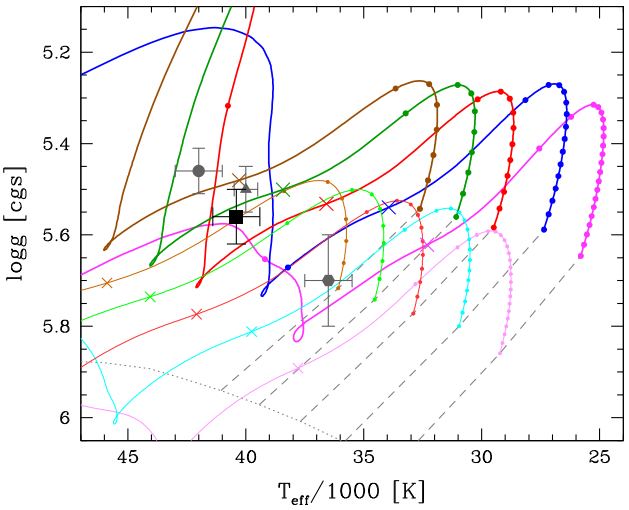

Figure 8. $T_{\rm eff}$–log g diagram with the position of EPIC 216747137 (square symbol) compared with the evolutionary tracks by Han et al. (2002) for different stellar masses: from right to left 0.45, 0.50, 0.55, 0.60, and 0.65 $M_\odot$, (magenta, blue, red, green, and brown respectively in the online version). The envelope mass is 0.005 $M_\odot$ (thick lines) or 0.001 (thin lines and light colours). Along the evolutionary tracks, the age differences between adjacent dots are 10^7 yr. The crosses mark the point of central helium exhaustion. Helium MS and zero-age EHB (ZAEHB) are shown as dotted and dashed lines respectively. The positions of the evolved HW Vir systems AA Dor (circle, Klepp & Rauch 2011) and V1828 Aql (triangle, Almeida et al. 2012) and of the evolved reflection-effect sdB+dM binary HS 2333+3927 (pentagon, Heber et al. 2004) are also reported. Note that AA Dor and V1828 Aql have masses of 0.47 and 0.42 $M_\odot$ respectively, and therefore should definitely be post-EHB [compare with the 0.45 $M_\odot$ (magenta) and 0.50 $M_\odot$ (blue) tracks].

has been derived from angular diameter and parallax, the mass ($0.56^{+0.11}_{-0.10}$ $M_\odot$) follows from gravity and the luminosity (100^{+16}_{-15} $L_\odot$) from radius and effective temperature.

A comparison with evolutionary models for EHB stars by Han et al. (2002) is shown in Fig. 8 and demonstrates that the hot subdwarf has likely just evolved beyond the core-helium-burning phase, similar to AA Dor (Klepp & Rauch 2011) and V1828 Aql (Almeida et al. 2012), or is at the very end of helium burning, depending on the hot subdwarf mass and envelope mass.

6 EPHEMERIS

First we computed independent ephemerides from photometric and RV data, obtaining a good agreement on the orbital period. The orbital period derived from the RVs has a higher precision thanks to the longer baseline (2.0 versus 1.6 yr) and also because of the poor time resolution of the *K*2 data. Then, considering both spectroscopic and photometric data together, we were able to remove the degeneracy due to the spectral windows and obtain a better determination of the orbital period thanks to the longer baseline (2.8 yr). In practice, taking as reference the center of the primary eclipse, we verified that the time difference between the last primary eclipse of our data set (determined from RVs) and the first one (determined from photometry) was very close to an integer multiple of the orbital period determined from the RVs. Then, imposing that such time difference is *exactly* a multiple of the orbital period, we obtain the best determination of the orbital period and the following best ephemeris:

$$\begin{aligned} \mathrm{BJD_{TDB}} &= (2457301.56346 \pm 0.00041) \\ &\quad + (0.16107224 \pm 0.00000017)\,\mathrm{E} \end{aligned}$$

where $\mathrm{BJD_{TDB}}$ is the barycentric Julian date of the centre of each primary eclipse using barycentric dynamical time (see e.g. Eastman, Siverd & Gaudi 2010).

7 MODELLING OF THE LIGHT CURVE

The SAAO *BRV* light curves show relatively deep eclipses together with a reflection effect with increasing amplitude from *B* to *R*, and a secondary eclipse only visible due to the reflection effect. Such a light curve is characteristic for sdO/B systems with close, cool, low-mass companions. For the modelling of the light curve we used LCURVE, a code written to model detached but also accreting binaries containing a WD (for details, see Copperwheat et al. 2010). It has been used to analyse several detached WD-M dwarf binaries (e.g. Parsons et al. 2010), which show very similar light curves with deep eclipses and a prominent reflection effect, if the primary is a hot WD. Recently, LCURVE was used also for an sdB+BD system (submitted Schaffenroth et al. 2020). The code subdivides each star into small elements with a geometry fixed by its radius as measured along the direction towards the other star. Roche distortions and irradiation are also included, as well as limb-darkening, gravitational darkening, lensing, Doppler beaming, Rømer delay, and asynchronous orbits. The latter three effects, lensing, Doppler beaming and Rømer delay, are not detectable in our light curves. The irradiation is approximated by assigning a new temperature to the heated side of the companion:

$$\sigma T_{\rm sec}'^4 = \sigma T_{\rm sec}^4 + F_{\rm irr} = \sigma T_{\rm sec}^4 \left[1 + \alpha \left(\frac{T_{\rm prim}}{T_{\rm sec}}\right)^4 \left(\frac{R_{\rm prim}}{a}\right)^2\right]$$

Table 4. Parameters of the light-curve fit of the SAAO *BVR*-band light curves for the best model.

Band	*B*	*V*	*R*
		Fixed parameters	
q		0.175	
P		0.1610732	
$T_{\rm eff,\,sdB}$		40400	
$x_{1,\,1}$	0.0469	0.0434	0.0379
$x_{1,\,2}$	0.2668	0.2346	0.2082
g_1		0.25	
g_2		0.08	
		Fitted parameters	
i	85.04 ± 0.40	85.62 ± 0.19	85.51 ± 0.14
r_1/a	0.1887 ± 0.0016	0.1890 ± 0.0008	0.1887 ± 0.0005
r_2/a	0.1251 ± 0.0028	0.1216 ± 0.0012	0.1222 ± 0.0009
$T_{\rm eff,\,comp}$	3000 ± 500	2965 ± 482	3042 ± 503
A_2	0.95 ± 0.08	1.01 ± 0.04	1.25 ± 0.04
x_2	0.33	0.27	0.28
T_0	2457892.53884	2457891.57235	2457893.66629
slope	0.004729	0.003015	0.00088
$\frac{L_1}{L_1+L_2}$	0.98028	0.972691	0.94864

with α being the Bond albedo of the companion and $F_{\rm irr}$ the irradiating flux, accounting for the angle of incidence and distance from the hot subdwarf. If the irradiation effect is very strong, the description given above might not be sufficient. The backside of the irradiated star is completely unaffected in this description, but heat transport could heat it up, increasing the luminosity of unirradiated parts as well.

Since the model contains many parameters, not all of them independent, we fixed as many parameters as possible (see Table 4). The sdOB temperature was fixed to the temperature determined from the spectroscopic fit. The gravitational darkening coefficients were fixed to the values expected for a radiative atmosphere for the primary (von Zeipel 1924) and a convective atmosphere for the secondary (Lucy 1967), using a blackbody approximation to calculate the resulting intensities. More sophisticated models such as those proposed by Espinosa Lara & Rieutord (2011) or Claret & Bloemen (2011, see also Claret et al. 2020) were not used because the deformations from a spherical shape are very small and in fact gravity darkening has almost no impact. For the limb darkening of the primary, we adopted a quadratic limb-darkening law using the tables by Claret & Bloemen (2011). As the tables include only surface gravities up to $\log g = 5$, we used the values closest to the parameters derived by the spectroscopic analysis. As the two stars are almost spherical (we do not see significant ellipsoidal deformations), the light curve is not sensitive to the mass ratio and therefore we computed solutions with different, fixed mass ratios. To localize the best set of parameters, we used a SIMPLEX algorithm (Press et al. 1992) varying the inclination, the radii, the temperature of the companion, the geometric albedo of the companion (A_2), the limb darkening of the companion, the period and the time of the primary eclipse. Moreover, we also allowed for corrections of a linear trend, which is often absorbed in observing hot stars, as the comparison stars are often redder and so the correction for the airmass is often insufficient (slope). The model of the best fit is shown in Fig. 9, together with the observations and the residuals.

To get an idea about the degeneracy of the light-curve solutions, as well as the errors of the parameters, we performed also Markov Chain Monte Carlo (MCMC) computations using the best solution obtained with the SIMPLEX algorithm as a starting value and varying the radii, the inclination, the temperature of the companion, as well as the albedo of the companion (Figs A1–A3). A clear correlation between the radius of the companion, the inclination, and the geometric albedo of the companion (A_2) can be seen, which results from the fact that the companion is only visible in the light curve due to the reflection effect and the amplitude depends on the inclination, the radius of the companion and the albedo, as well as the separation and temperature and radius of the primary, which is given by the spectroscopic analysis.

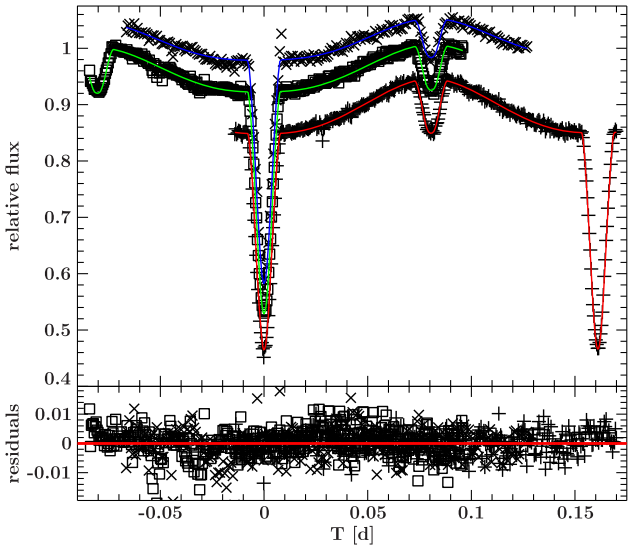

Figure 9. Normalized SAAO $B(\times)$, $V(\square)$, and $R(+)$-band light curves together with the best fit. For better visualization, the *V*- and *R*-band light curves have been shifted. The lower panel shows the residuals.

8 NATURE OF THE COMPANION

As stated before, it is not possible to derive the mass ratio from the light-curve analysis. Since we have only a single-lined system, it is necessary to look for other possibilities to constrain the mass ratio of the system. Taking into account the sdOB atmospheric parameters obtained from our spectroscopic analysis, the sdOB star is likely an evolved post-EHB star or just at the end of helium burning, depending on the hot subdwarf mass and envelope mass.

When we combine the analysis of the RV and the light curves, we get different masses and radii of both components, as well as a different separation for each solution with a different mass ratio. From the spectroscopic analysis we derived the surface gravity of the hot subdwarf, which can be compared to a photometric surface gravity calculated from the mass and radius derived from the light-curve analysis and the mass function. Moreover, from the radius determined by the *Gaia* parallax and the SED fit, we can calculate a *Gaia* surface gravity. The comparison of the photometric, spectroscopic, and *Gaia* surface gravity is shown in Fig. 10. An agreement is seen for a mass between ∼0.47 and ∼0.67 $M_\odot$. This means a post-EHB hot subdwarf with a canonical mass of 0.47 $M_\odot$ cannot be excluded.

Another possibility to constrain the masses further is to consider the mass–radius relation of the companion (Fig. 11), and compare it to theoretical predictions (Baraffe et al. 2003; Chabrier & Baraffe 1997). Using the mass–radius relation for the cool companion, the best agreement is found for an sdOB mass of ∼0.62 $M_\odot$. This is hence the most consistent solution, that implies a ∼2 per cent inflation of

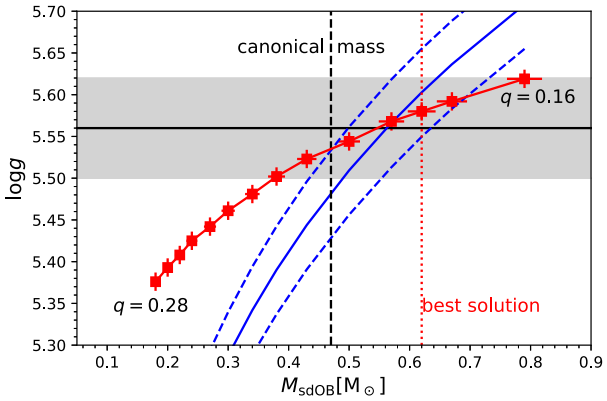

Figure 10. Mass of the sdOB versus the photometric log g for different mass ratios from 0.16 to 0.28 in steps of 0.1 (adding 0.175 for the best solution). They were derived from combining the results from the analysis of the light curve and RV curve. The grey area marks the spectroscopic log g that was derived by the spectroscopic analysis. The blue lines mark the surface gravity derived from the radius determined by the *Gaia* parallax and the SED fit. The vertical lines represent the two solutions which are given in Table 5.

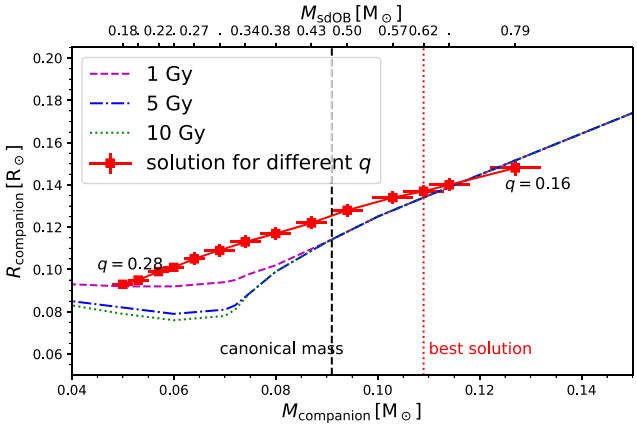

Figure 11. Comparison of theoretical mass–radius relations of BDs by Baraffe et al. (2003) and low-mass M dwarfs by Chabrier & Baraffe (1997) for an age of 1 Gyr (dashed), 5 Gyr (dotted–dashed), and 10 Gyr (dotted) to results from the light-curve analysis. Each error cross represents a solution from the light-curve analysis for a different mass ratio ($q = 0.16$–0.28 in steps of 0.1 and adding 0.175 for the best solution). The vertical lines represent the two solutions of Table 5.

the M-dwarf radius. A lower mass would imply a more inflated radius for the M dwarf.

In Table 5, we consider two solutions (absolute system parameters) of the light-curve analysis resulting from two different assumptions on the mass ratio q. A massive one at $q = 0.175$, corresponding to an sdOB mass of 0.62 $M_\odot$, which we prefer because it avoids strong inflation of the companion, and a second solution at $q = 0.194$, which corresponds to the canonical mass ($M = 0.47$ $M_\odot$). For the preferred solution of a high-mass post-EHB star, we obtain a companion mass of 0.109 ± 0.004 $M_\odot$, corresponding to a low-mass M dwarf. For a canonical mass sdOB, the mass of the M star would be even less (0.091 ± 0.003 $M_\odot$), only slightly above the stellar mass limit.

9 SUMMARY AND DISCUSSION

EPIC 216747137 is a new HW Vir system that belongs to the small subgroup of eclipsing hot subdwarf binaries in which the primary is a hot, evolved, sdOB star. The other two members of this

Table 5. Absolute parameters of the system.

	Best solution	Post-EHB canonical
q	0.175	0.194
a ($R_\odot$)	1.121 ± 0.028	1.028 ± 0.025
M_{sdOB} ($M_\odot$)	0.620 ± 0.023	0.470 ± 0.017
M_{comp} ($M_\odot$)	0.109 ± 0.004	0.091 ± 0.003
R_{sdOB} ($R_\odot$)	0.212 ± 0.005	0.194 ± 0.005
R_{comp} ($R_\odot$)	0.137 ± 0.003	0.125 ± 0.003
log g_{phot} (cgs)	5.58 ± 0.01	5.54 ± 0.01

group, AA Dor and V1828 Aql, with a mass of 0.47 and 0.42 $M_\odot$ respectively (Klepp & Rauch 2011; Almeida et al. 2012), should definitely be post-EHB stars (and this is particularly true for AA Dor that has been intensively studied by various teams). While for EPIC 216747137, due to its larger mass of ∼0.62, we can just say that it is close, and likely beyond, central helium exhaustion.

Among the 20 published HW Vir systems, only AA Dor, V1828 Aql, and EPIC 216747137 have effective temperatures near 40 kK, while all the others have T_{eff} between 25 and 35 kK, compatible with He-core burning (Wolz et al. 2018). Moreover, these three hotter HW Vir systems seem to follow a different relation in the T_{eff}–log y plane (Edelmann et al. 2003) respect to all the other HW Vir stars. The position of all the published HW Vir in a T_{eff}–log y plane can be seen in Wolz et al. (2018, fig. 5). Since the number of new HW Vir systems is rapidly increasing, with 25 new systems already spectroscopically confirmed and many more to come (Schaffenroth et al. 2019), the larger statistics will allow us to confirm or not that HW Vir stars follow two different sequences in the T_{eff}–log y plane.

The orbital period of EPIC 216747137, ∼0.161 d, and the mass of its dM companion, ∼0.11 $M_\odot$, fit well with the period distribution and the companion mass distribution of the hot subdwarf binaries with a dM companion (Figs 7 and 8, Kupfer et al. 2015). However, in the preferred light-curve solution, the sdOB mass is unusually high (0.62 $M_\odot$). Such a high mass could result from post-AGB evolution, but this possibility is ruled out because it would imply a luminosity 10 times higher than observed. When we consider constraints from spectroscopy, light-curve solution and parallax, the mass must be between 0.47 and 0.67 $M_\odot$. Hence a mass as low as 0.47 $M_\odot$ cannot be ruled out, but it implies that the cool companion is significantly inflated. Although inflation in M dwarfs is not a well understood phenomenon (see e.g. Parsons et al. 2018), a strong inflation appears quite unlikely, and this is why we prefer the high-mass option.

A mass as high as ∼0.62 $M_\odot$ provides a challenge for the hot subdwarf formation theories since the CE ejection channel struggles to form stars with a mass higher than ∼0.47, while the RLOF channel does not work for orbital periods shorter than ∼1 d (see e.g. figs 10 and 12, respectively, Han et al. 2003).

Another interesting aspect of our results is that EPIC 216747137 is not synchronized. Among the other nine systems with published rotational velocities, only three of them are not synchronized (submitted, and references therein Schaffenroth et al. 2020), all of them being relatively young and not evolved (and with a BD candidate companion, but this might be related to a selection effect considering that it is easier to obtain high-resolution data when the companion is a BD), while the other six more evolved systems are all synchronized. The growing number of synchronized systems seems in contradiction with the prediction by Preece, Tout & Jeffery (2018) that synchronization time-scales are longer than the sdB lifetime.

Hot subdwarf stars are found in all stellar populations (Martin et al. 2017; Luo, Németh & Li 2020). EPIC 216747137 lies just 155 pc below the Galactic plane. This hints at thin disc membership.

In order to check this assumption, we carried out a kinematical investigation calculating Galactic trajectories in a Galactic potential (for details, see Appendix B). The Galactic orbit is almost perfectly circular and the binary orbits within (though close to) the solar circle (Fig. B1). Hence, we conclude that the binary belongs to the thin disc population, which is also confirmed by its position in the Toomre diagram (Fig. B2).

ACKNOWLEDGEMENTS

The *K*2 data presented in this paper was obtained from the Mikulski Archive for Space Telescopes (MAST). Space Telescope Science Institute is operated by the Association of Universities for Research in Astronomy, Inc., under NASA contract NAS5-26555. This paper uses observations made at the SAAO. The spectroscopic results are based on observations collected at the MPG/ESO 2.2- m telescope; at the 2.6-m NOT, operated jointly by Denmark, Finland, Iceland, Norway, and Sweden; and at the 6.5-m Magellan I telescope. RS acknowledges financial support from the INAF project on 'Stellar evolution and asteroseismology in the context of the PLATO space mission' (PI: S. Cassisi). VS is supported by the Deutsche Forschungsgemeinschaft, DFG through grant GE 2506/9-1. DK thanks the University of the Western Cape and the National Research Foundation of South Africa for financial support. We thank Jantje Freudenthal for support at the SAAO 1 -m Elizabeth telescope, Michel Rieutord and an anonymous referee for useful comments. RS wishes to remember and thank Nicolò D'Amico, President of INAF, who suddenly passed away a few days before the submission of this article.

DATA AVAILABILITY

The data underlying this article will be shared on reasonable request to the corresponding author.

REFERENCES

Alam S. et al., 2015, ApJS, 219, 12
Allen C., Santillan A., 1991, Rev. Mex. Astron. Astrofis., 22, 255
Almeida L. A., Jablonski F., Tello J., Rodrigues C. V., 2012, MNRAS, 423, 478
Auer L. H., Mihalas D., 1972, ApJS, 24, 193
Bailer-Jones C. A. L., Rybizki J., Fouesneau M., Mantelet G., Andrae R., 2018, AJ, 156, 58
Baraffe I., Chabrier G., Barman T. S., Allard F., Hauschildt P. H., 2003, A&A, 402, 701
Baran A. S., Bachulski S., Curyło M., 2016, IAU Focus Meeting, 29B, 497
Beauchamp A., Wesemael F., Bergeron P., 1997, ApJS, 108, 559
Brahm R., Jordán A., Espinoza N., 2017, PASP, 129, 034002
Chabrier G., Baraffe I., 1997, A&A, 327, 1039
Chambers K. C., et al., 2017, The Pan-STARRS release 1 (PS1) Survey - DR1 : II/349, available at https://cdsarc.unistra.fr/viz-bin/cat/II/349,
Charpinet S. et al., 2011, Nature, 480, 496
Charpinet S., Giammichele N., Zong W., Van Grootel V., Brassard P., Fontaine G., 2018, Open Astron., 27, 112
Claret A., Bloemen S., 2011, A&A, 529, A75
Claret A., Cukanovaite E., Burdge K., Tremblay P. E., Parsons S., Marsh T. R., 2020, A&A, 634, A93
Clausen D., Wade R. A., 2011, ApJ, 733, L42
Clausen D., Wade R. A., Kopparapu R. K., O'Shaughnessy R., 2012, ApJ, 746, 186
Copperwheat C. M., Marsh T. R., Dhillon V. S., Littlefair S. P., Hickman R., Gänsicke B. T., Southworth J., 2010, MNRAS, 402, 1824
Wright E. L., et al., 2010, AJ, 140, 1868
Drechsel H. et al., 2001, A&A, 379, 893
Eastman J., Siverd R., Gaudi B. S., 2010, PASP, 122, 935
Edelmann H., Heber U., Hagen H. J., Lemke M., Dreizler S., Napiwotzki R., Engels D., 2003, A&A, 400, 939
Espinosa Lara F., Rieutord M., 2011, A&A, 533, A43
Evans D. W. et al., 2018, A&A, 616, A4
Fitzpatrick E. L., Massa D., Gordon K. D., Bohlin R., Clayton G. C., 2019, ApJ, 886, 108
Fontaine G., Brassard P., Charpinet S., Green E. M., Randall S. K., Van Grootel V., 2012, A&A, 539, A12
Fouqué P. et al., 2000, A&AS, 141, 313
Fuhrmann K., 2004, Astron. Nachr., 325, 3
Geier S. et al., 2011, ApJ, 731, L22
Giddings J. R., 1981, PhD thesis Univ. London
Han Z., Podsiadlowski P., Maxted P. F. L., Marsh T. R., Ivanova N., 2002, MNRAS, 336, 449
Han Z., Podsiadlowski P., Maxted P. F. L., Marsh T. R., 2003, MNRAS, 341, 669
Han Z., Chen X., Lei Z., Podsiadlowski P., 2012, in Kilkenny D., Jeffery C. S., Koen C., eds, ASP Conf. Ser. Vol. 452, Fifth Meeting on Hot Subdwarf Stars and Related Objects. Astron. Soc. Pac., San Francisco, p. 3
Heber U., 2016, PASP, 128, 966
Heber U. et al., 2004, A&A, 420, 251
Heber U., Irrgang A., Schaffenroth J., 2018, Open Astron., 27, 35
Henden A. A., Levine S., Terrell D., Welch D. L., 2015, in American Astronomical Society Meeting Abstracts #225. p. 336.16
Hirsch H. A., 2009, PhD thesis, Friedrich-Alexander University Erlangen-Nürnberg
Hubeny I., Hummer D. G., Lanz T., 1994, A&A, 282, 151
Irrgang A., Wilcox B., Tucker E., Schiefelbein L., 2013, A&A, 549, A137
Irrgang A., Kreuzer S., Heber U., Brown W., 2018, A&A, 615, L5
Kelson D. D., 2003, PASP, 115, 688
Kelson D. D., Illingworth G. D., van Dokkum P. G., Franx M., 2000, ApJ, 531, 159
Klepp S., Rauch T., 2011, A&A, 531, L7
Kramer M., Schneider F. R. N., Ohlmann S. T., Geier S., Schaffenroth V., Pakmor R., Roepke F. K., 2020, A&A, 642, A97
Kupfer T. et al., 2015, A&A, 576, A44
Kupfer T. et al., 2020, ApJ, 891, 45
Kurucz R. L., 1996, in Adelman S. J., Kupka F., Weiss W. W., eds, ASP Conf. Ser. Vol. 108, Model Atmospheres and Spectrum Synthesis. Astron. Soc. Pac., San Francisco, p. 160
Lawrence A. et al., 2007, MNRAS, 379, 1599
Lindegren L. et al., 2018, A&A, 616, A2
Lucy L. B., 1967, Z. Astrophys., 65, 89
Luo Y., Németh P., Li Q., 2020, ApJ, 898, 64
Maíz Apellániz J., Weiler M., 2018, A&A, 619, A180
Martin P., Jeffery C. S., Naslim N., Woolf V. M., 2017, MNRAS, 467, 68
Maxted P. F. L., Heber U., Marsh T. R., North R. C., 2001, MNRAS, 326, 1391
Napiwotzki R., Green P. J., Saffer R. A., 1999, ApJ, 517, 399
Napiwotzki R., Karl C. A., Lisker T., Heber U., Christlieb N., Reimers D., Nelemans G., Homeier D., 2004, Ap&SS, 291, 321
Onken C. A. et al., 2019, PASA, 36, e033
Parsons S. G., Marsh T. R., Copperwheat C. M., Dhillon V. S., Littlefair S. P., Gänsicke B. T., Hickman R., 2010, MNRAS, 402, 2591
Parsons S. G. et al., 2018, MNRAS, 481, 1083
Pauli E. M., Napiwotzki R., Heber U., Altmann M., Odenkirchen M., 2006, A&A, 447, 173
Pelisoli I., Vos J., Geier S., Schaffenroth V., Baran A. S., 2020, A&A, 642, A180
Preece H. P., Tout C. A., Jeffery C. S., 2018, MNRAS, 481, 715
Press W. H., Teukolsky S. A., Vetterling W. T., Flannery B. P., 1992, Numerical Recipes in FORTRAN. The Art of Scientific Computing, 2nd edn. Cambridge Univ. Press, Cambridge
Ratzloff J. K. et al., 2020, ApJ, 890, 126
Reed M. D. et al., 2018, Open Astron., 27, 157
Saffer R. A., Bergeron P., Koester D., Liebert J., 1994, ApJ, 432, 351
Schaffenroth V., Geier S., Heber U., Kupfer T., Ziegerer E., Heuser C., Classen L., Cordes O., 2014, A&A, 564, A98

Schaffenroth V., Barlow B. N., Drechsel H., Dunlap B. H., 2015, A&A, 576, A123
Schaffenroth V. et al., 2019, A&A, 630, A80
Schaffenroth V. et al., 2020, MNRAS, preprint (arXiv:2011.10013)
Schechter P. L., Mateo M., Saha A., 1993, PASP, 105, 1342
Schlafly E. F., Finkbeiner D. P., 2011, ApJ, 737, 103
Schlafly E. F., Meisner A. M., Green G. M., 2019, ApJS, 240, 30
Schlegel D. J., Finkbeiner D. P., Davis M., 1998, ApJ, 500, 525
Silvotti R. et al., 2014, A&A, 570, A130
Silvotti R., Østensen R. H., Telting J. H., 2020, preprint (arXiv:2002.04545)
Soker N., 1998, AJ, 116, 1308
Stark M. A., Wade R. A., 2003, AJ, 126, 1455
Telting J., Østensen R., Reed M., Kiæerad F., Farris L., Baran A., Oreiro R., O'Toole S., 2014, in van Grootel V., Green E., Fontaine G., Charpinet S., eds, ASP Conf. Ser. Vol. 481, 6th Meeting on Hot Subdwarf Stars and Related objects. Astron. Soc. Pac., San Francisco, p. 287
Tremblay P. E., Bergeron P., 2009, ApJ, 696, 1755
von Zeipel H., 1924, MNRAS, 84, 665
Wolf C. et al., 2018, PASA, 35, e010
Wolz M. et al., 2018, Open Astron., 27, 80
Wood J. H., Saffer R., 1999, MNRAS, 305, 820

APPENDIX A: MCMC FITS OF THE SAAO BVR LIGHT CURVES

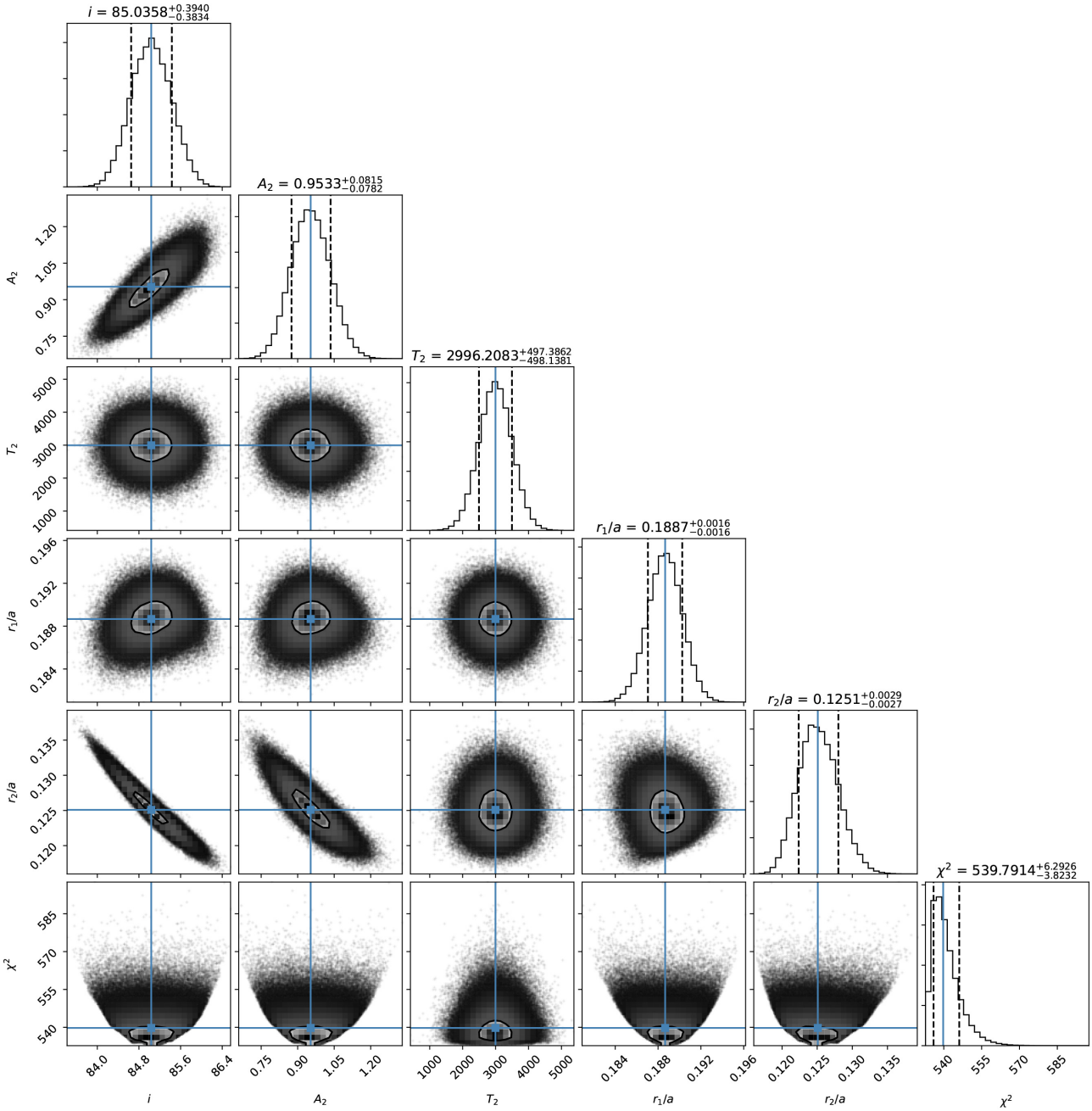

Figure A1. MCMC computations showing the degeneracy and the parameter errors of the *B*-band light-curve solutions.

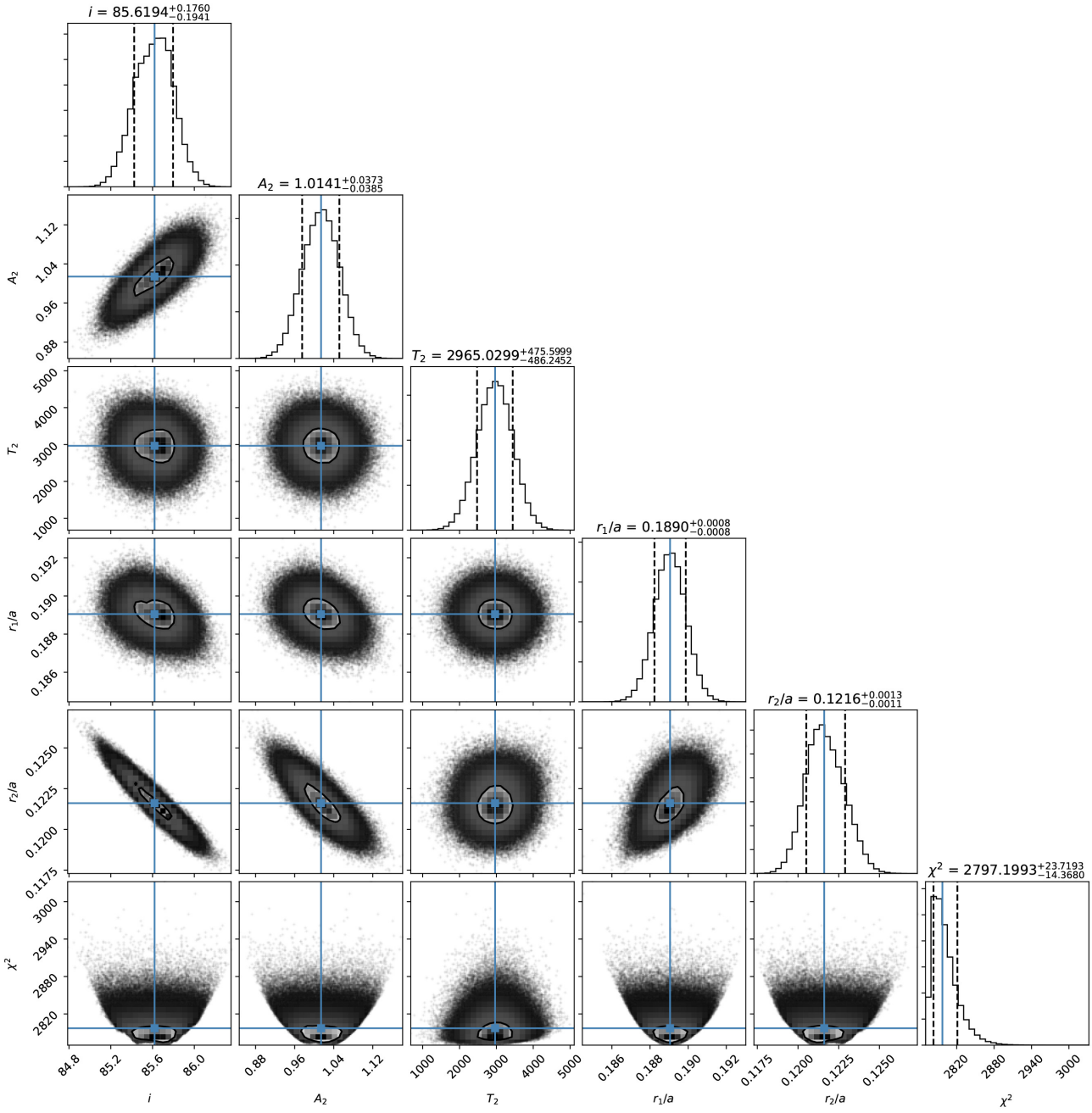

Figure A2. Same as Fig. A1, but for the *V*-band light curve.

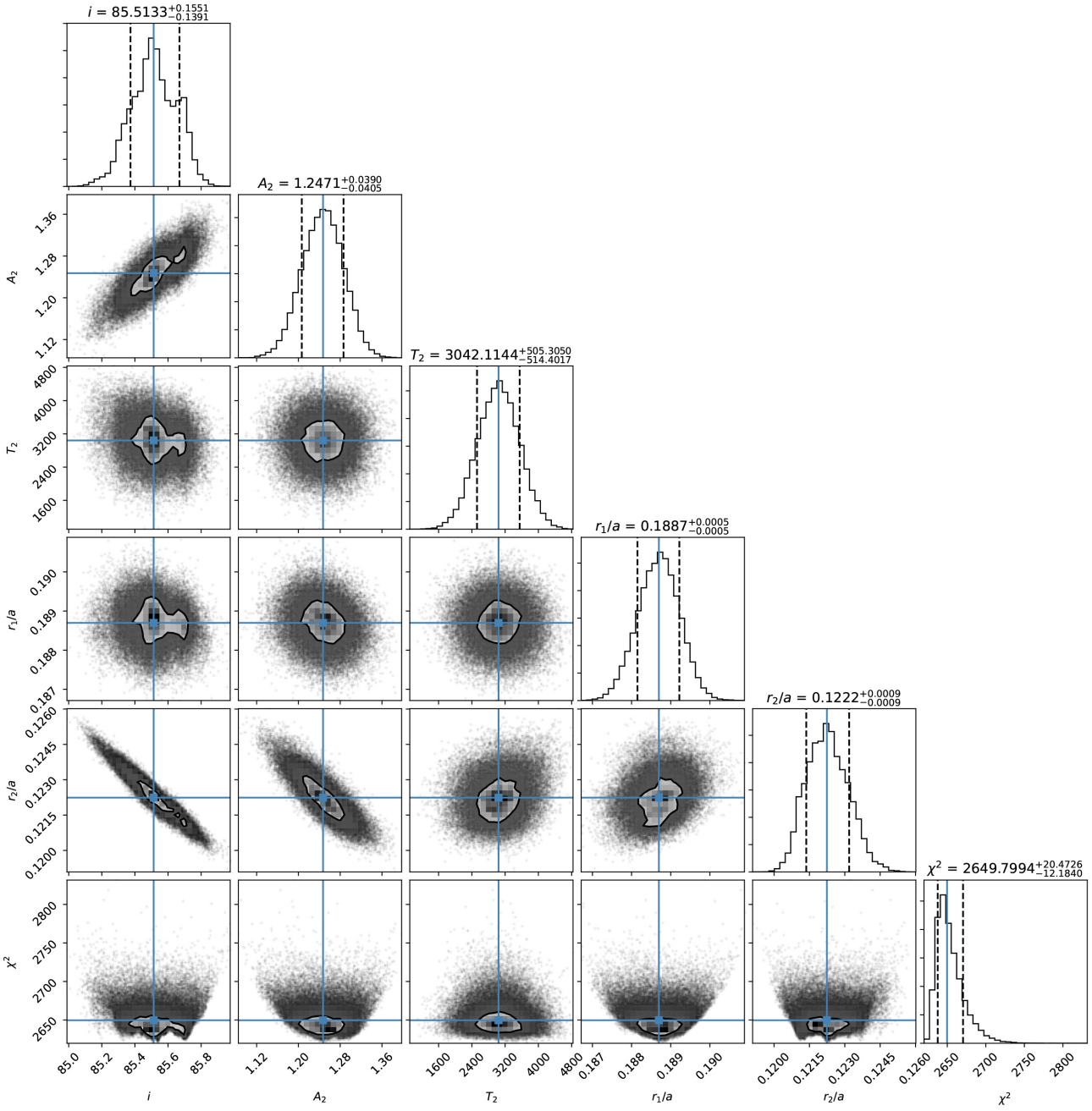

Figure A3. Same as Fig. A1, but for the *R*-band light curve.

APPENDIX B: KINEMATICS OF EPIC 216747137

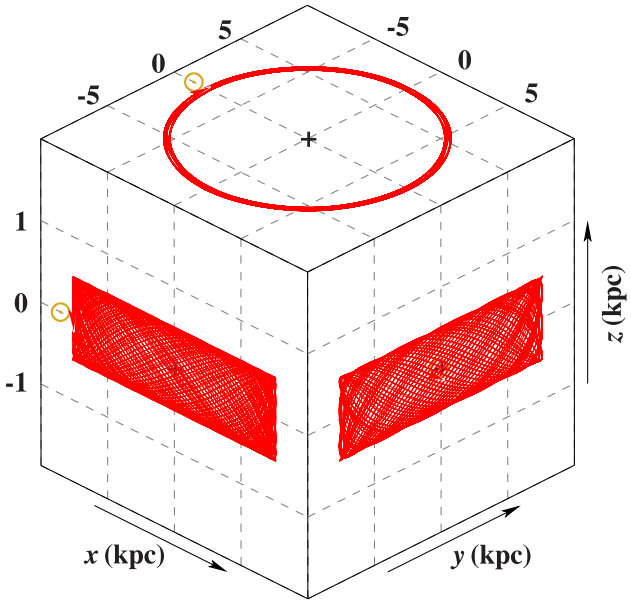

Figure B1. EPIC 216747137's 3D orbit in a Cartesian Galactic coordinate system. The centre of the Galaxy lies at the origin, the Sun (yellow circled dot) on the negative x-axis. The z-axis points to the Galactic north pole. Trajectories were computed back in time for 10 Gyr using a standard, axisymmetric model for the Galactic gravitational potential (an updated version of that of Allen & Santillan 1991, see Irrgang et al. 2013, for details). The shape of the orbit is almost circular, with vertical oscillations of a few hundred pc amplitude, typical for a thin-disc star (see e.g. Pauli et al. 2006).

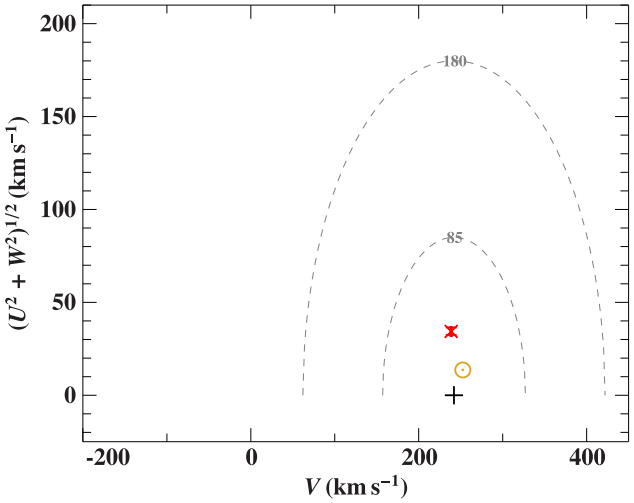

Figure B2. The position of EPIC 216747137 (red cross with 1σ error bars) in the Toomre diagram. The velocity component V is measured in the direction of the rotation of the Galaxy, U towards the Galactic centre, and W perpendicular to the plane. The yellow circled dot marks the position of the Sun. The local standard of rest (LSR) is marked by a plus sign. According to Fuhrmann (2004), the boundaries for thin and thick discs are located at 85 and 180 km s^{-1}, respectively (dashed circles centred around the LSR).

This paper has been typeset from a TEX/LATEX file prepared by the author.